PERGAMON

PII: S1359-6454(99)00266-9

Acta mater. Vol. 47, Nos 15, pp. 4061–4068, 1999
Published by Elsevier Science Ltd
On behalf of Acta Metallurgica Inc.
Printed in Great Britain
1359-6454/99 $20.00 + 0.00

DIRECT ATOMIC-SCALE IMAGING OF CERAMIC INTERFACES

E. C. DICKEY[1], X. FAN[1, 2] and S. J. PENNYCOOK[2]†

[1]Department of Chemical and Materials Engineering, University of Kentucky, Lexington, KY 40506-0046, U.S.A. and [2]Solid State Division, Oak Ridge National Laboratory, Oak Ridge, TN 37831, U.S.A.

Abstract—Understanding the atomic structure and chemistry of internal interfaces is often critical to developing interface structure–property relationships. Results are presented from several studies in which Z-contrast scanning transmission electron microscopy (STEM) and electron energy loss spectroscopy (EELS) have been employed to solve the atomic structures of oxide interfaces. The Z-contrast imaging technique directly reveals the projected cation sublattices constituting the interface, while EELS provides chemical and local electronic structure information. Because Z-contrast imaging and EELS can be performed simultaneously, direct correlations between structure and chemistry can be made at the atomic scale. The utility of Z-contrast imaging and EELS is demonstrated in three examples: a ZrO_2 24° [100] symmetric tilt grain boundary, a NiO–cubic ZrO_2 eutectic interface and a Ni–cubic ZrO_2 metal–ceramic interface. The power and versatility of Z-contrast and EELS for solving interface structures in oxide systems is clearly demonstrated in these three material systems. *Published by Elsevier Science Ltd on behalf of Acta Metallurgica Inc.*

Keywords: Ceramic; Interface; Scanning transmission electron microscopy (STEM); Electron energy loss spectroscopy (EELS)

1. INTRODUCTION

The structure and chemistry of interfaces are known to affect the mechanical and electrical behaviors of oxide ceramics [1, 2]. It is therefore useful to obtain experimental data regarding the atomic structure and chemistry of these interfaces that can be used as the basis of atomistic simulations [3, 4]. Z-contrast STEM imaging has become increasingly popular among materials scientists for structure determination because the images are more directly interpretable than conventional high-resolution TEM images. Z-contrast imaging is an incoherent imaging process; thus the phase ambiguity inherent to HREM images is removed. Moreover, because the high-angle, or Rutherford scattered, electrons are used for image formation, there is chemical sensitivity in the images. For oxide materials, Z-contrast imaging has been a useful technique for understanding interface structures and defects. In particular, Z-contrast images directly reveal the projected cation sublattices of the material. While almost no information about the oxygen positions is contained in the Z-contrast images, positions can often be inferred or EELS can provide some information regarding the local coordination around oxygen atoms. One caveat for obtaining atomic-scale structural data by Z-contrast imaging, or in fact by any electron imaging technique, is that the two phases constituting the interface must have crystallographic orientation relationships that lead to the parallel alignment of low-index zone axes. Z-contrast imaging is particularly sensitive to crystal tilt since it necessitates channeling conditions. If, however, the two crystals are well oriented, then atomic-scale images and spectra can be obtained along the common zone axes of the two crystals.

Below we present case studies from three classes of oxide interfaces: (1) a grain boundary, (2) an oxide–oxide heterophase interface and (3) a metal–oxide heterophase interface. The three examples have a common attribute in that they all contain yttria-stabilized cubic ZrO_2 as one of the constituent phases (all references to ZrO_2 below are to cubic ZrO_2). The grain boundary is a ZrO_2 24° symmetric tilt [100] grain boundary. The NiO–ZrO_2 interfaces are formed by directional solidification of a NiO–ZrO_2 eutectic, and the Ni–ZrO_2 interfaces are formed by the reduction of the NiO–ZrO_2 eutectic. In all three cases, atomic-scale models of the interfaces are generated from Z-contrast images.

2. EXPERIMENTAL TECHNIQUES

All Z-contrast imaging studies were carried out on the 300 kV VG Microscopes HB603U dedicated STEM ($C_s = 1$ mm) at Oak Ridge National Laboratory. In the Z-contrast imaging technique, transmitted electrons are detected by a high-angle annular dark field detector. Although the electron scattering process in STEM has both coherent and

†To whom all correspondence should be addressed.

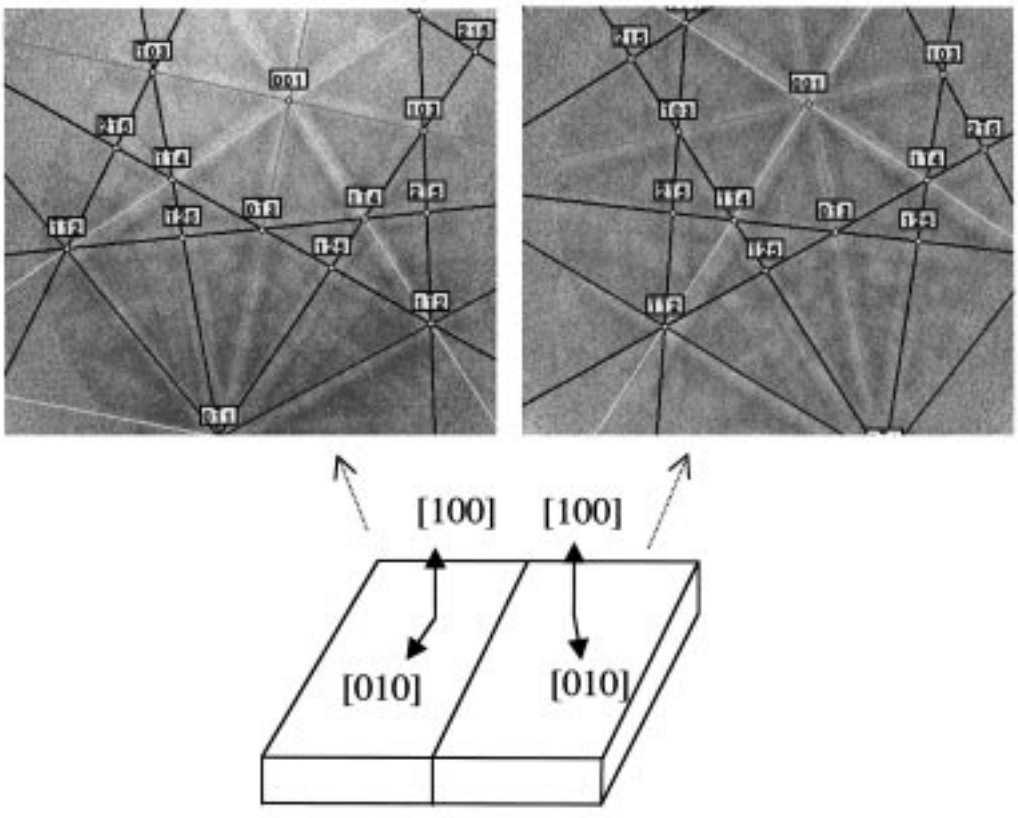

Fig. 1. Electron backscattered diffraction patterns from a 24° symmetric tilt [100] ZrO_2 bicrystal.

incoherent (thermal diffuse scattering) components, a transversely incoherent image can be produced by the large-angle annular detector which effectively breaks the transverse coherence of the signal by averaging over the interference fringes in the transverse plane [5, 6]. Because the signal is incoherent, the intensity in a Z-contrast image, $I(\mathbf{R})$, is given by the convolution of the incident probe intensity, $P^2(\mathbf{R})$, with the crystal object function, $O(\mathbf{R})$:

$$I(\mathbf{R}) = O(\mathbf{R}) * P^2(\mathbf{R}).$$

Even under dynamical diffraction conditions, it has been shown that s-type Bloch states, which are tightly bound to individual atomic columns, are predominantly responsible for the image intensity [7–9]. Consequently, the object function is localized on atomic columns. It should also be noted that the cross sections for scattering to high angles are much greater for higher atomic number elements so that the Z-contrast image intensity scales with atomic number, producing peaks of intensity at the cation sites while yielding almost no intensity at low-Z column positions [6].

Maximum entropy reconstructions were performed to quantify atomic positions from the Z-contrast images [10, 11]. Using a Lorentzian profile for the probe function, $P^2(\mathbf{R})$, the object function, $O(\mathbf{R})$, corresponding to cation positions was reconstructed by maximum entropy image analysis [12, 13]. The resulting object function was used for quantitative analysis. Note that all object functions presented below are convoluted with a Gaussian for better visibility.

To assess the positional accuracy of the technique, images of the perfect crystal, far from any defect, were analyzed. The object function positions were compared to the known atomic column positions based on the crystal structure and a standard deviation (σ_d) between the two positions was calculated. Positional accuracies do depend on signal-to-noise ratios in the image and therefore vary with imaging conditions and the scattering power of the material [13]. Reference [13] gives a thorough review of the factors that affect the accuracy of reconstructed Z-contrast images. In $SrTiO_3$ the $3\sigma_d$ for Sr columns is 0.019 nm and for Ti columns (having less scattering power) is 0.024 nm [13]. In the [112] NiO lattice projection, discussed below, we find that object functions derived from images recorded at a magnification of 10^7 times yield positional accuracies ($3\sigma_d$) of 0.021 nm far away from the interface. Although the ultimate accuracy of reconstructed Z-contrast images is consistently found to be on the order of 0.02 nm for cation col-

umns, STEM images, because they are serially acquired, are susceptible to mechanical and electronic instabilities. Any such perturbations will, of course, distort the lattice image and degrade the positional accuracy.

To characterize the chemistry of the interfaces, EEL spectra were collected on a 100 kV HB501UX STEM. Because an annular dark field image may be acquired simultaneously, the probe could be positioned accurately to provide EEL spectra from well-defined areas of the specimen. The energy resolution of the parallel energy loss spectrometer, as determined by the full-width half-maximum of the zero-loss peak, was 1.1 eV and the dispersion was 0.303 eV/channel over 385 channels. Each spectrum was corrected for the gain variation across the detector array and the background was fitted to a power law over a 50 eV window preceding the edge-onset and subtracted from each spectrum.

The 24° symmetric tilt [100] ZrO_2 bicrystal used in this study was purchased in bulk from Shinkosha Co. Ltd, Japan. Backscattered electron diffraction patterns shown in Fig. 1 illustrate and confirm the orientation relationship between the two crystals. Specimens were prepared normal to the tilt axis, along [100].

The NiO–ZrO_2 eutectic interfaces were produced by directional solidification as described elsewhere [14, 15]. Each grain within the bulk eutectic sample contains lamellae of the two phases which have well-defined crystallographic orientation relationships:

$$[1\bar{1}0]_{NiO}//[100]_{ZrO_2}//\text{growth direction}$$

$$[111]_{NiO}//[010]_{ZrO_2}.$$

Cross-sectional samples were prepared from two orthogonal directions so that the three-dimensional structure of the interface could be examined.

The Ni–ZrO_2 interfaces were formed by reducing the NiO–ZrO_2 eutectics [16]. The reductive phase transformation is electrochemical in nature and results in oxygen removal from NiO to the outside gas phase through the fast-ion conducting ZrO_2. The Ni remains well aligned crystallographically with respect to the ZrO_2 although a twin of the cation sublattice results from the phase transformation (see Ref. [17] for details). The final orientation relationship between the Ni and ZrO_2 is

$$[\bar{1}10]_{Ni}//[100]_{ZrO_2}$$

$$[111]_{Ni}//[010]_{ZrO_2}.$$

Cross-sectional samples were prepared along the $[\bar{1}10]_{Ni}//[100]_{ZrO_2}$ orientation.

All of the TEM samples were prepared by mechanically thinning interface cross sections to approximately 10 μm. For the heterophase interfaces, it was crucial that the samples be <10 μm thick before ion milling because of the differential thinning rates of the two phases. The cross sections were subsequently ion milled to electron transparency with 5 keV Ar^+ ions at liquid nitrogen temperature. To remove any amorphous surface layers, the foils were finally milled with 3 keV Ar^+ ions.

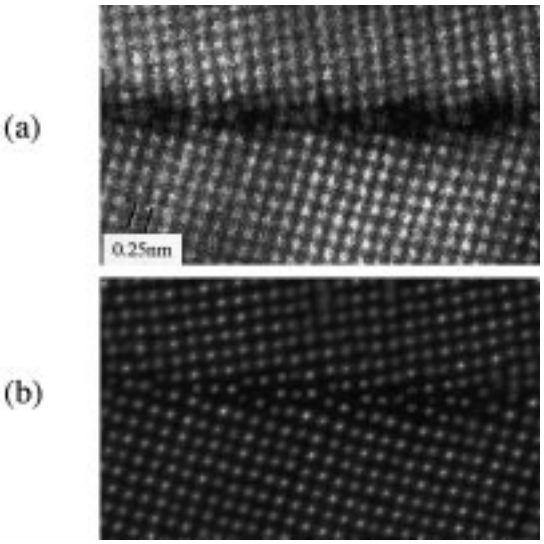

Fig. 2. Atomic-scale image of 24° symmetrical [100] tilt cubic-ZrO_2 boundary: (a) Z-contrast STEM image; (b) object function derived from maximum entropy reconstruction.

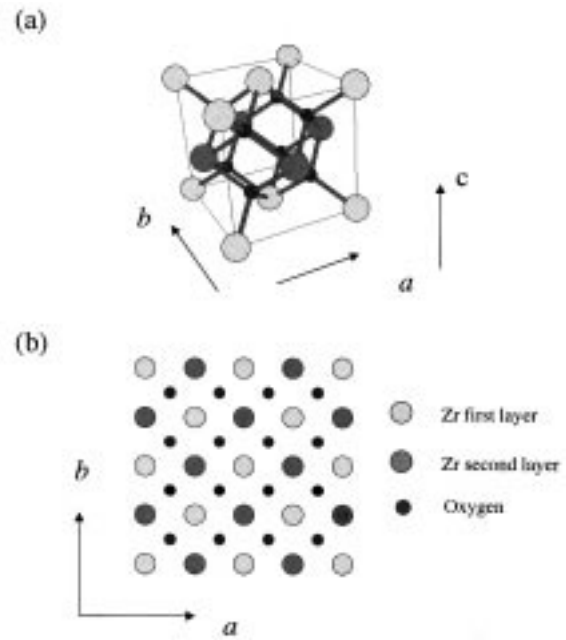

Fig. 3. Unit cell of ZrO_2: (a) perspective view; (b) [001] projection. Notice that [001] has two different Zr layers a half unit cell apart. We distinguish them by two shades of gray.

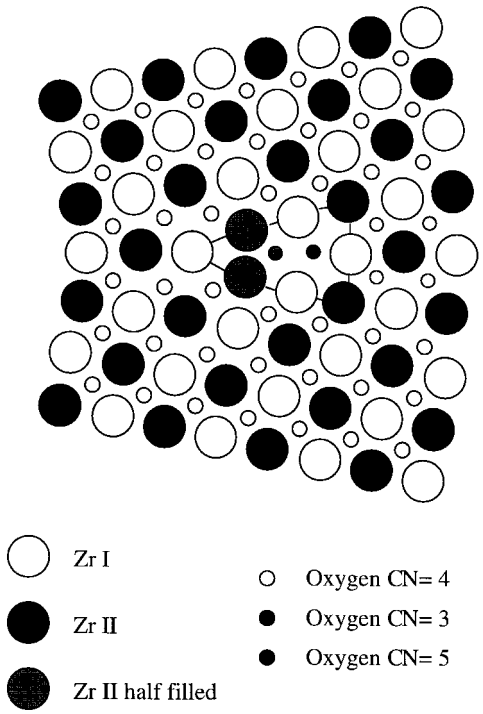

Fig. 4. Boundary structure model determined from Z-contrast image. Cation sites are determined directly by maximum entropy, oxygen sites are assumed. The solid lines outline the defect structural unit which is stoichiometric and therefore uncharged.

3. RESULTS AND DISCUSSION

3.1. 24° ZrO_2 tilt boundary

The Z-contrast image of the 24° symmetric tilt [100] ZrO_2 grain boundary is shown in Fig. 2 along with the corresponding object function obtained by maximum entropy reconstruction. The white dots in the image correspond to Zr columns, or the cation sublattice. Within the field of view, the 24° tilt boundary is composed of a periodic array of a basic structural unit (these are indicated by the open circles on Fig. 2). Since the image is only a representation of the projected structure, it is important to appreciate the cubic-ZrO_2 crystal structure (fluorite structure) in three dimensions. Figure 3 shows a ZrO_2 unit cell in which the Zr atoms are distinguished by their position along the [100] direction, the beam direction. The Zr atoms denoted in dark gray are a half unit cell below the Zr atoms in light gray.

Based on the Z-contrast images, a structural model of the grain boundary was developed and is shown in Fig. 4. Between each structural unit, there is a continuity of the (200) planes across the boundary indicating no in-plane rigid body translation. Within the defect structural unit, two of the Zr columns (both having Zr atoms at the same depth) are very close to each other in the boundary core. Electrostatically, this situation would be energetically unfavorable because of the close proximity of the Zr cations. However, also note that the intensities of these two columns in Fig. 2 are lower than those of the other Zr columns. The lower intensities can be interpreted as partially occupied Zr columns. Partial occupancy would allow the Zr atoms in the two adjacent columns to stagger along the beam direction and thus avoid close cation–cation positions. Similar observations have been made in other grain boundary studies including those of $SrTiO_3$ [18, 19] and $YBa_2Cu_3O_{7-x}$ [20]. Partial oc-

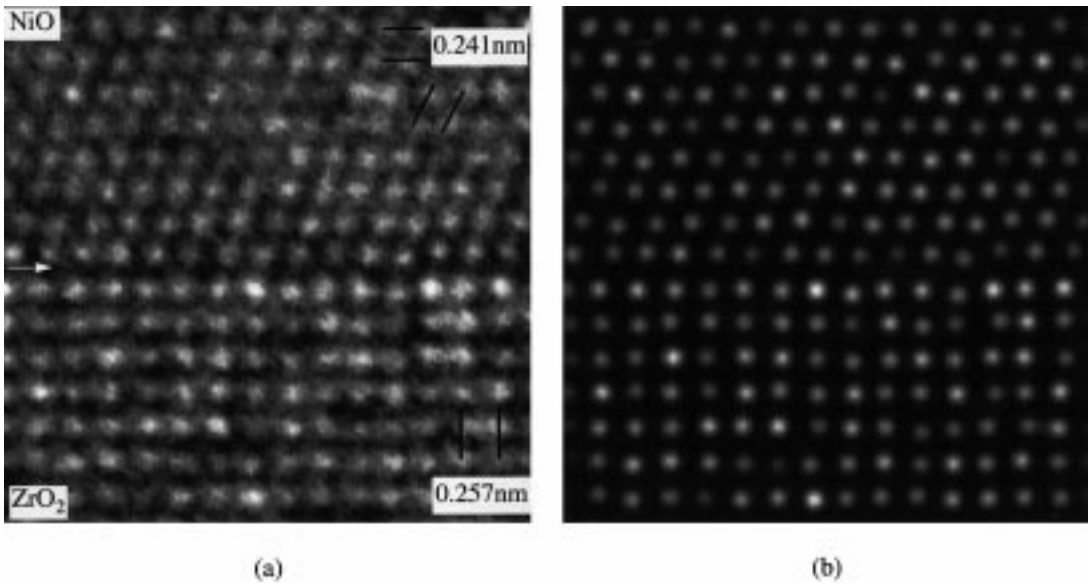

Fig. 5. Atomic-scale image of NiO–ZrO_2 interface along $[1\bar{1}0]_{NiO}//[100]_{ZrO_2}$: (a) Z-contrast STEM image; (b) object function derived from maximum entropy reconstruction.

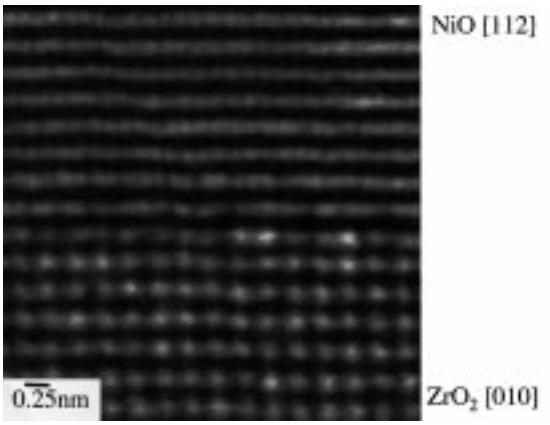

Fig. 6. Z-contrast image of NiO–ZrO_2 interface along $[112]_{NiO}//[010]_{ZrO_2}$ reveals displacement of the Ni atoms from their bulk lattice sites near the interface.

cupancy to avoid cation crowding is emerging as a common relaxation mechanism for oxide grain boundaries.

The oxygen positions in the grain boundary model were chosen such that they were most similar to the positions in bulk ZrO_2. In the fluorite structure, the oxygen ions are tetrahedrally coordinated by Zr ions. Most of the oxygen sites near the boundary have very similar environments to bulk oxygen sites in that they maintain a distorted tetrahedral coordination (these are indicated in white in Fig. 4). In the core of the structural unit, if we assume full oxygen columns, then the number of nearest neighbors would vary from that observed in the bulk. The oxygen sites indicated in gray in Fig. 4 would be deficient in Zr nearest neighbors while those shown in black would have an excess of nearest neighbors. Since the Z-contrast image does not give us information regarding the oxygen ions, it will be necessary to further explore the coordination of the oxygen ions at the boundary core with a combination of EELS and atomistic simulations. Having accurate coordinates for the cation positions from the Z-contrast image, however, provides a good starting model of the interface from which further refinements can be made.

3.2. NiO–ZrO_2 heterophase interfaces

As a result of the crystallographic orientation relationship between NiO and ZrO_2, it was possible to image the edge-on interface along two orthogonal directions, allowing a three-dimensional model of the interface to be produced [15]. Figure 5 shows the Z-contrast image of the NiO–ZrO_2 interface along the $[1\bar{1}0]_{NiO}//[100]_{ZrO_2}$ projection. The bright spots, again, correspond to the projected cation sublattices. Note that even though the atomic number of Zr is 40 and Ni is 28, the intensities of the Zr and Ni columns are very similar. This is because the atomic density of the Zr columns is much less than that of the Ni columns. The image shows that the interface is atomically flat and abrupt with a separation of 0.271 ± 0.004 nm between the interface Ni and Zr planes. This spacing is larger than that of either Zr (200) or NiO (111), so some volume expansion at the interface plane is observed. The boundary appears completely coherent with no misfit dislocations—the lattice misfit along this direction is only 0.4%.

Although the interface appears extremely ordered and coherent along the projection discussed above, the same is not true in three dimensions. When viewed along an orthogonal projection,

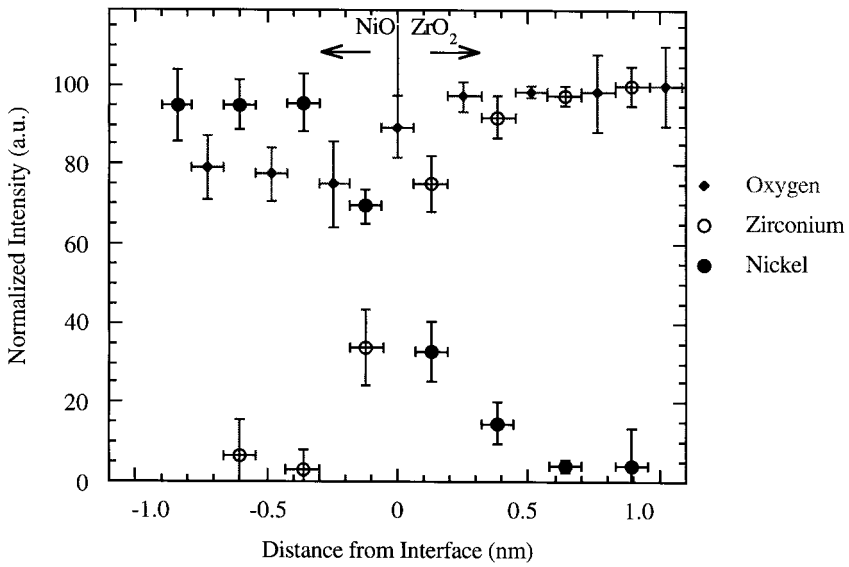

Fig. 7. EELS elemental profiles taken in steps of interplanar spacing across a NiO–ZrO_2 interface.

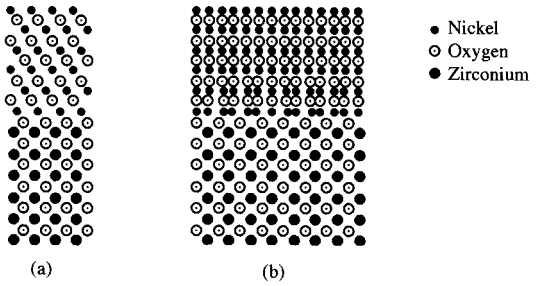

Fig. 8. Three-dimensional model of the NiO–ZrO_2 interface derived from Z-contrast images: (a) $[1\bar{1}0]_{NiO}//[100]_{ZrO_2}$ projection; (b) $[112]_{NiO}//[010]_{ZrO_2}$ projection.

$[112]_{NiO}//[010]_{ZrO_2}$, where there is a 14% lattice mismatch between the two lattices, structural disorder is observed near the boundary predominantly in the NiO (see Fig. 6). The NiO $(2\bar{2}0)$ lattice fringes running perpendicular to the interface have a 0.148 nm spacing that was successfully imaged by the VG HB603U machine. When the atomic positions are determined from maximum entropy reconstructions, a 0.02 nm root mean square (r.m.s.) relaxation of the $(2\bar{2}0)_{NiO}$ in the plane adjacent to the boundary is quantified. Because the interface is incommensurate along this direction, the relaxation is aperiodic.

EELS profiles acquired in steps of interplanar spacing across the interface indicate that the boundary is chemically abrupt as well. Figure 7 shows the chemical profiles, determined from integrated core-loss EELS edges for the various elements, in steps of interplanar spacing across the interface. Note that there is a complete transition from NiO to ZrO_2 in two interplanar steps, indicating no appreciable intermixing between the two phases across the boundary plane. The oxygen intensity at the interface is intermediate to that of either phase.

A three-dimensional model of the boundary based on the experimental data is shown in Fig. 8. Note several salient features of the model. First, the boundary consists of a single oxygen plane that is shared between the two crystals and continues the anion–cation sequence of planes seamlessly across the interface. Secondly, this common oxygen plane, as projected along $[1\bar{1}0]_{NiO}//[100]_{ZrO_2}$, is continuous with the oxygen sublattices of both phases, suggesting that the anion sublattice, and not the cation sublattice, is controlling the rigid body translation. Finally, the r.m.s. strain in the NiO along $[1\bar{1}0]_{NiO}$ has been incorporated into the model. Although the projected strains are on the order of 15%, the interatomic distances change by a maximum of $\pm$4.6%. The model not only provides us with an accurate, experimentally based interpretation of the interface structure, but also demonstrates the necessity of obtaining three-dimensional information from heterophase interfaces. Although Z-contrast images only provide two-dimensional data, as has been illustrated, if more than one edge-on cross section can be made, three-dimensional information from the interface can be obtained.

3.3. *Ni–ZrO_2 interface*

The interface between Ni and ZrO_2 [17] provides another challenge not yet encountered in the oxide–oxide interfaces. Because the ZrO_2 (100) surface is polar, it can terminate at the Ni–ZrO_2 interface with either an O or Zr plane. The former would result in Ni–O bonds across the boundary and the latter in Ni–Zr bonds. Figure 9 shows a Z-contrast

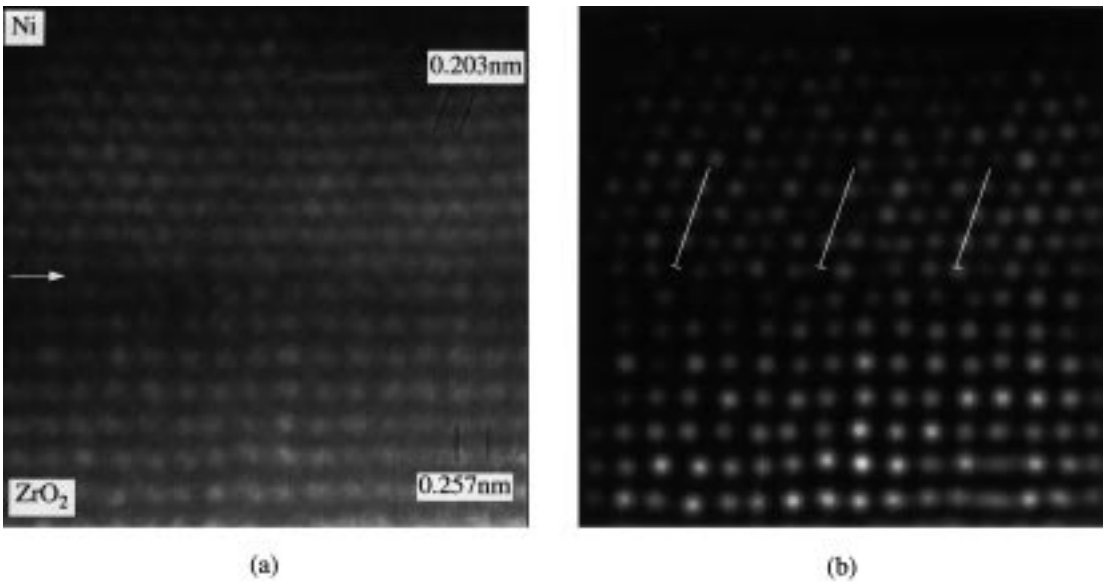

Fig. 9. Z-contrast STEM image of interface between Ni and ZrO_2 along $[110]_{Ni}//[100]_{ZrO_2}$.

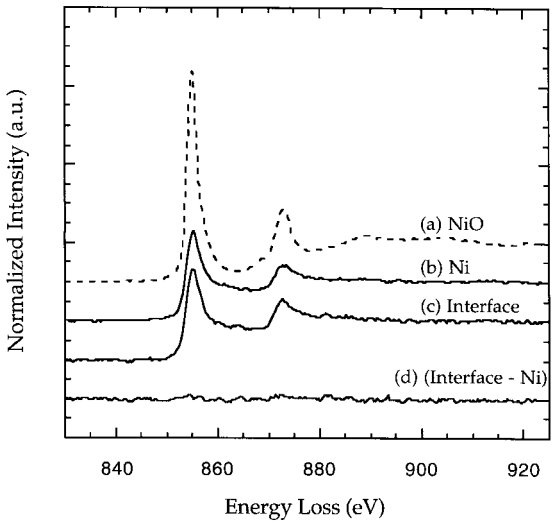

Fig. 10. Ni $L_{2,3}$ EEL spectra from: (a) bulk NiO; (b) bulk Ni; (c) the Ni–ZrO_2 interface. All spectra have been normalized to the contribution from the continuum. Spectrum d, the difference spectrum, results from subtracting the bulk Ni spectrum (b) from the interface spectrum (c).

image of the Ni–ZrO_2 interface along with the maximum entropy reconstruction along the $[1\bar{1}0]_{Ni}$ zone axis. Upon reduction, there is now a substantial 17% lattice mismatch between the two phases that leads to the misfit dislocations identified in Fig. 9.

Although the image does directly reveal the presence or absence of oxygen between the terminating Ni and Zr planes at the interface, the interplanar spacing between the two cation planes does provide some indirect evidence. The spacing between the terminating Ni and Zr planes was quantified from the maximum entropy reconstruction and found to be 0.244 ± 0.004 nm. This compares to a spacing of 0.271 ± 0.004 nm in the oxide–oxide boundary before reduction. The substantial contraction at the interface suggests that oxygen has been lost from the boundary plane. To substantiate this contention, we also collected EELS spectra from the boundary plane to investigate the type of bonding present at the interface. A metal–oxygen bond should show some ionicity while a metal–metal bond would not. We used the Ni $L_{2,3}$ EELS edge as a signature since its fine structure is very sensitive to the valence state of the Ni (see Fig. 10). The L_3/L_2 ratio of Ni^{2+} is 20–30% greater than that of metallic Ni [21–23]. The L_3 peak is also much sharper and more symmetrical in NiO than Ni due to the presence of a core exciton in the oxide [23]. As shown in Fig. 10, the EELS spectrum from the interface plane is nearly identical to the metallic Ni reference spectrum and therefore shows no evidence for an ionic bond at the interface. This is consistent with the observed contraction in the boundary plane observed in the Z-contrast images. We can

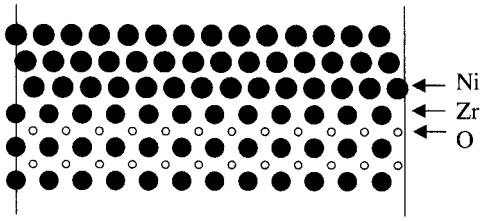

Fig. 11. Unrelaxed structure of Ni–ZrO_2 interface illustrating metal–metal termination at the boundary.

therefore conclude that metal–metal bonding predominates at this interface. Unfortunately, for this interface it was not possible to obtain lattice images from two edge-on boundary orientations. Although the $[010]_{ZrO_2}$ and $[112]_{Ni}$ zone axes are parallel, the $(220)_{Ni}$ lattice spacing is below the spatial resolution of the instrument. Based on the available data, however, an unrelaxed boundary structure was developed that incorporates the metal–metal termination at the interface; this is shown in Fig. 11.

4. CONCLUSIONS

As illustrated in the previous three examples, Z-contrast STEM imaging is an extremely powerful technique for elucidating the atomic structures of oxide interfaces. When coupled with maximum entropy analysis, quantitative structural information can be extracted. Structural units comprising grain boundaries can be directly determined from object function coordinates. Because the scattered cross sections scale with atomic number, partially occupied columns can be identified from lower intensities. When multiple edge-on projections of an interface can be obtained, Z-contrast images can provide quantitative three-dimensional structural information including rigid body translations and local atomic relaxations. In the case of metal–oxide interfaces, accurate determination of interplanar spacings can be obtained by maximum entropy analysis and can distinguish between metal and oxygen termination. Atomic resolution EELS is a powerful complementary means for quantifying atomic bonding at such interfaces. The experimentally based atomic models will serve as excellent starting models for atomistic calculations that can give further insight into the physical properties of the interfaces.

REFERENCES

1. Norton, M. G. and Carter, C. B., in *Materials Interfaces*, ed. D. Wolf and S. Yip. Chapman & Hall, London, 1992, pp. 151–189.
2. Dimos, D., *Phys. Rev. B*, 1990, **41**, 4038.
3. Yan, Y., Chisholm, M. F., Duscher, G. and Pennycook, S. J., *Phys. Rev. Lett.*, 1998, **81**, 3675.

4. Pennycook, S. J., Dickey, E. C., Nellist, P. D., Chisholm, M. F., Yan, Y. and Pantelides, S. T., *J. Eur. Ceram. Soc.*, 1999, **19**, 2211
5. Jesson, D. E. and Pennycook, S. J., *Proc. R. Soc. Lond. A*, 1993, **441**, 261.
6. Jesson, D. E. and Pennycook, S. J., *Proc. R. Soc. Lond. A*, 1995, **449**, 273.
7. Pennycook, S. J. and Jesson, D. E., *Acta metall. mater.*, 1992, **40**, S149.
8. Pennycook, S. J. and Jesson, D. E., *Phys. Rev. Lett.*, 1990, **64**, 938.
9. Pennycook, S. J. and Jesson, D. E., *Ultramicroscopy*, 1991, **37**, 14.
10. Gull, S. F. and Daniell, G. J., *Nature*, 1978, **272**, 686.
11. Gull, S. F. and Skilling, J., *IEE Proc.*, 1984, **131F**, 646.
12. Nellist, P. D. and Pennycook, S. J., *J. Microsc.*, 1998, **190**, 159.
13. McGibbon, A. J., Pennycook, S. J. and Jesson, D. E., *J. Micros.*, 1999, **195**, 44
14. Dhalenne, G. and Revcolevschi, A., *J. Cryst. Growth*, 1984, **69**, 616.
15. Dickey, E. C., Dravid, V. P., Nellist, P. D., Wallis, D. J. and Pennycook, S. J., *Acta mater.*, 1998, **46**, 1801.
16. Revcolevschi, A. and Dhalenne, G., *Nature*, 1985, **316**, 335.
17. Dickey, E. C., Dravid, V. P., Nellist, P. D., Wallis, D. J., Pennycook, S. J. and Revcolevschi, A., *Microsc. Microanal.*, 1997, **3**, 443.
18. McGibbon, M. M., Browning, N. D., Chisholm, M. F., McGibbon, A. J. and Pennycook, S. J., *Science*, 1994, **261**, 102.
19. McGibbon, M. M., Browning, N. D., McGibbon, A. J. and Pennycook, S. J., *Phil. Mag. A*, 1996, **73**, 625.
20. Browning, N. D., Nellist, P. D., Norton, D. P., Chisholm, M. F. and Pennycook, S. J., *Physica C*, 1998, **294**, 183.
21. Waddington, W. G., Rez, P., Grant, I. P. and Humphreys, C. J., *Phys. Rev. B*, 1986, **34**, 1467.
22. Sparrow, T. G., Williams, B. G., Ral, C. N. R. and Thomas, J. M., *Chem. Phys. Lett.*, 1984, **108**, 547.
23. Leapman, R. D., Grunes, L. A. and Fejes, P. L., *Phys. Rev. B*, 1982, **26**, 614.